arXiv:1211.6922v1 [astro-ph.HE] 29 Nov 2012

Prepared for submission to JCAP

# The sensitivity of Cherenkov telescopes to dark matter and astrophysically induced anisotropies in the diffuse gamma-ray background

**Joachim Ripken,[a] Alessandro Cuoco,[a] Hannes-S. Zechlin,[b] Jan Conrad,[a] Dieter Horns[b]**

[a]The Oskar Klein Centre for Cosmo Particle Physics, AlbaNova,
SE-106 91 Stockholm, Sweden
[b]University of Hamburg, Institut für Experimentalphysik,
Luruper Chaussee 149, D-22761 Hamburg, Germany

E-mail: ripken@fysik.su.se, cuoco@fysik.su.se,
hzechlin@physik.uni-hamburg.de, conrad@fysik.su.se,
dieter.horns@physik.uni-hamburg.de

**Abstract.** In this work, we investigate in detail the capabilities of present (H.E.S.S., MAGIC, VERITAS) and planned (CTA) ground-based Cherenkov telescope systems to detect angular anisotropies in the diffuse gamma-ray background. We first study the impact of instrumental characteristics (effective area, field of view, angular resolution, and background rejection efficiency) to the ability to detect anisotropies. In addition, we compare different observation strategies, i.e., whether a single deep observation or a splitting over multiple shallow fields is preferred. Secondly, the sensitivity to anisotropies generated by self-annihilating dark matter is investigated for different common dark matter models. With planned configurations of CTA, we find that a relative contribution of $\sim 10\%$ from dark matter annihilation to the diffuse gamma-ray background can be detected, together with the sensitivity to the self-annihilation cross section $\langle \sigma v \rangle = 3 \times 10^{-26}\,\mathrm{cm^3 s^{-1}}$ expected from thermal dark matter freeze-out. We also stress the importance of constraining anisotropies from unresolved astrophysical sources already with the current generation of instruments, as a novel and complementary method to constrain the properties of TeV sources.

## Contents

**1 Introduction** **1**

**2 Optimizing the observation strategy** **3**
2.1 Simplified setup 3
2.2 Influence of the detector configuration 4

**3 Benchmark instrumental setups and cosmic-ray backgrounds** **8**

**4 Dark matter sensitivity** **10**

**5 Discussion and Conclusions** **16**

**A Error on the Poisson Anisotropy** **17**
A.1 Simple calculation 17
A.2 More accurate calculation 18

**B Sensitivity using the intensity APS** **19**

**C Sensitivity using the fluctuation APS** **20**

## 1 Introduction

The study of gamma-ray anisotropies [1, 2] is recently providing new and complementary insights into the nature of gamma-ray sources and the diffuse gamma-ray background (DGB) [3, 4]. The pattern of anisotropies has been studied with different techniques, mainly through its Angular Power Spectrum (APS), as in [1, 2]. Likewise, the study of the 1-point Probability Distribution Function (PDF) [5] and the cross-correlation with galaxy catalogues [6] provides further complementary information.

It has been argued that Dark Matter (DM) self-annihilation or decay can leave a peculiar imprint into the anisotropy pattern and spectrum of the DGB [7–18]. In fact, while the emissivity of ordinary astrophysical sources scales with their inner densities $\sim \varrho$ (modulo a source-class dependent bias factor), the emissivity of self-annihilating DM scales with its density squared $\sim \varrho^2$. Owing to this difference, self-annihilating DM could leave a characteristic imprint in the anisotropy power spectrum of the DGB. This simple picture, however, can be spoilt by the presence of unresolved point sources which produce a Poisson-like APS, more closely resembling the DM one. Nonetheless, even if the astrophysical Poissonian term dominates the intrinsic clustering APS and, thus, the astrophysical and dark matter APS look indeed similar, it is still possible to separate the two contributions by looking at the energy dependence of the APS, i.e. looking at the *anisotropy energy spectrum* [13]. The different hypotheses about the origin of the DGB can thus be tested by measuring the angular power spectrum together with its energy dependence.

At the same time, theoretical predictions for the anisotropies generated by different gamma-ray source populations (e.g., blazars and galaxy clusters [19], millisecond pulsars [20], star-forming galaxies [21]) are becoming available, contributing to clarify and extend our knowledge of this approach and its potential.

At present, gamma-ray radiation is detected mainly through two techniques. Observatories in space, such as the Fermi Large Area Telescope (Fermi-LAT) [22], detect gamma-rays through pair conversion in the detector itself. Fermi-LAT observes gamma-ray photons in the energy range from $\sim 20\,\mathrm{MeV}$ up to a few hundred GeV, with an effective area close to $1\,\mathrm{m}^2$ and a field of view (fov) of $\sim 1\,\mathrm{sr}$. Fermi-LAT routinely operates in sky surveying mode, continuously mapping the entire sky. On the other hand, ground-based Cherenkov telescopes like the current experiments H.E.S.S. [23], MAGIC [24], and VERITAS [25], or the planned Cherenkov telescope array (CTA) [26, 27] observe the Cherenkov light produced by air showers initiated by gamma-rays in the upper atmosphere. The effective collection area of ground-based instruments is typically of the order of $10^5$–$10^6$ $\mathrm{m}^2$. The energy range of the current experiments covers about 60 GeV to 100 TeV, but future realizations of this concept will lower the threshold to 10 GeV or even 5 GeV [28]. Contrary to Fermi-LAT, ground-based instruments cover only a relatively small field of view of typically a few msr, so that all-sky scans are not feasible. Observations are possible only during the night and in conditions of clear sky reducing the duty-cycle to about 10%. Furthermore, the trigger rate is dominated by a large background of hadronic showers. Specific techniques are employed to reduce this background substantially. However, even after sufficient gamma-hadron separation, air showers induced by cosmic-ray electrons can still substantially contribute to the background at a few hundred GeV [29–32], hardly separable from photon-induced air showers. Despite the above mentioned difficulties, interesting scales for the investigation of anisotropies are typically very small (less than $1^\circ$), so that the small field of view is not a serious limit for their study. The angular resolution of Cherenkov telescopes is typically better than $0.1^\circ$, so that multipoles in the range 100–1000 can be easily resolved. At the same time, the background is expected to be isotropic at small scales and thus also not a fundamental obstacle.

In this paper, we investigate in detail the capabilities of ground-based Cherenkov telescopes to measure gamma-ray angular anisotropies. In Section 2, we introduce a simplified Monte-Carlo approach, that we use to study the impact of instrumental characteristics (fov, angular resolution, and background rejection power) to the detection sensitivity for anisotropies. Since it would be very effective to analyze all the data collected from several observations taken for other scientific goals, we then investigate the influence of the *observation strategy* – whether it would be advantageous or disadvantageous to split the data into several fov. In Section 3 we list the instrumental setups that we use as benchmarks and we provide estimates of the CR background expected for these configurations. In Section 4, we use a more realistic simulation setup and study the sensitivity to anisotropies from DM self-annihilation using different DM models. We provide final comments and discussion in Section 5.

## 2 Optimizing the observation strategy

### 2.1 Simplified setup

As a measure of the anisotropy we will use the angular power spectrum (APS) of fluctuations throughout this paper. Given a map $I(\vartheta, \varphi)$ on the sphere, the fluctuation map is defined as $\delta(\vartheta, \varphi) = I(\vartheta, \varphi)/\bar{I} - 1$, where $\bar{I}$ is the mean value of $I$. The fluctuation map $\delta(\vartheta, \varphi)$ is then decomposed into spherical harmonics $Y^{\ell}_{m}(\vartheta, \varphi)$ as $\delta(\vartheta, \varphi) = \sum_{\ell m} a_{\ell m} Y^{\ell}_{m}(\vartheta, \varphi)$, where $a_{\ell m}$ are the coefficients of the spherical harmonic decomposition and $m = -l, \ldots, l$. From the $a_{\ell m}$, the APS is defined as

$$C_\ell \equiv \langle |a_{\ell m}|^2 \rangle, \tag{2.1}$$

where $\langle \ldots \rangle$ indicates the statistical ensemble average. Then, the quantity

$$\hat{C_\ell} = \sum_m \frac{|a_{\ell m}|^2}{2l+1} \tag{2.2}$$

is an unbiased estimator of the true power spectrum $C_\ell$, i.e. $\langle \hat{C_\ell} \rangle = C_\ell$.

Note that instead of the fluctuation dimensionless APS, the dimension-full APS of anisotropies (the APS of the map $I(\vartheta, \varphi)$ itself) can be used. This is particularly useful when analyzing real data (see [1]), but it will not be considered in the following.

In order to simulate a list of events containing anisotropies, we generate sky maps with a given $C_\ell$ spectrum. $C_\ell$ can be interpreted as the width of the $a_{\ell m}$ distribution over $m$ for fixed $\ell$. Assuming Gaussian fluctuations, the $a_{\ell m}$ for a fixed value of $\ell$ can be randomly chosen from a Gaussian distribution with mean 0 and width $\sqrt{C_\ell}$. The phase is chosen equally distributed between 0 an $2\pi$ with the condition $a_{\ell m} = a^{\star}_{-\ell m}$, to ensure fluctuation maps with real values. For a given spectrum, we generate twelve realizations of the $a_{\ell m}$ and thus twelve independent fluctuation maps of $\delta(\vartheta, \varphi)$. Moreover, we simulate maps with five different APS following a power law with slopes $s = 0.5$, 1.0, 1.5, 2.0, 2.5, i.e. $\ell(\ell+1)C_\ell \sim \ell^s$. The angular resolution of the simulated sky maps is chosen to be $0.002°$, corresponding to a maximum resolvable multipole $\ell = 9 \times 10^4$. The maps are normalized as $\delta'(\vartheta, \varphi) = (\delta(\vartheta, \varphi) - \delta_{\mathrm{min}})/(\delta_{\mathrm{max}} - \delta_{\mathrm{min}})$, in order to obtain a distribution between 0 and 1 to simulate events. Therefore, the map $\delta'$ acts as an effective intensity map $I'(\vartheta, \varphi) \equiv \delta'(\vartheta, \varphi)$. Note that the anisotropies of this effective intensity map are independent of the original $\delta(\vartheta, \varphi)$ normalization and always in the range $-1 < \delta I'/\bar{I}' < 1$, thus giving large fluctuations of the order of 100%. The setup has been optimized for the purpose of investigating the effects of instrumental characteristics on the APS. We will, however, extend the setup in Section 4, where we use a more realistic simulation of anisotropies, allowing to choose the desired anisotropy level.

Based upon the template intensity maps $I'(\vartheta, \varphi)$, the simulation of events requires a choice of three parameters: $\sigma_{\mathrm{fov}}$, the half-width of the camera acceptance, $\sigma_{\mathrm{psf}}$, the width of the point-spread function (PSF), and the signal fraction $f_{\mathrm{sig}}$, the fraction of signal events with respect to the sum of signal and background events. Event lists will contain a *signal* component (anisotropic) and a *background* component (isotropic by definition). Both, the camera acceptance as well as the PSF are assumed to follow Gaussian distributions.

Each event of the list is handled in three subsequent steps: The celestial position is chosen randomly according to the fov. Comparing a uniform deviate with $f_{\rm sig}$, it is then decided whether the event is handled as a *signal* or a *background* event. If the event belongs to the background, the event is just retained. In the signal case, instead, a variate $z$ is generated following a normalized uniform distribution. If $z$ is smaller than $I'(\vartheta,\varphi)$ at the event's position, the event is kept, and otherwise is rejected. Finally, each event is randomly displaced from its original direction according to the PSF, to realize the convolution of the map with the PSF. If not particularly specified, an event list will contain $N_{\rm event} = 10^7$ entries. We remark that this number is unrealistically high, even for CTA, and is just used to isolate and emphasize instrumental effects. Realistic numbers of signal and background events are provided in the next section.

We use the HEALPix software and pixelization scheme [34] to create and analyze count maps (with $N_{\rm pix}$ pixels), and to extract the APS. Before the analysis, the count map is cast into a fluctuation map

$$\delta''(\vartheta,\varphi) = -1 + \frac{N_{\rm pix}}{N_{\rm event}} \sum_{i=1}^{N_{\rm pix}} x_i \, b_i(\vartheta,\varphi), \tag{2.3}$$

where $x_i$ denotes the number of events in pixel $i$, and $b_i(\vartheta,\varphi)$ equals 1 inside pixel $i$ and 0 outside. In this way, $\delta''(\vartheta,\varphi)$ is normalized such that $\int \mathrm{d}\Omega \ (1+\delta''(\vartheta,\varphi)) = 4\pi$. Strictly speaking, $\delta''(\vartheta,\varphi)$ does not represent a fluctuation map, a factor of $f_{sky} = \Omega_{fov}/4\pi$ being required for the correct normalization. However, the above normalization ensures that the derived APS is already corrected for the incomplete sky coverage effect, at least at high multipoles [1]. Also note that we are directly analyzing the fluctuation map build out of the raw count map, while, in principle, the fluctuation map build from the reconstructed flux map (the count map divided by the exposure of the experiment or the fov in this case) can be analyzed. While the latter would be preferable for a real data analysis, the former is sufficiently accurate for a sensitivity study. It implies the extracted APS to be a convolution of the experiment's windowing function (the APS of the camera acceptance) with the true signal. Moreover, for the large $\ell$ considered below the windowing effect is marginal.

The statistical uncertainty of the APS is derived from the twelve simulations performed. In the following plots, the mean and the RMS as estimate of the standard deviation are shown as uncertainty bands.

### 2.2 Influence of the detector configuration

In Fig. 1, examples of recovered APS derived from the maps simulated with a given input APS slope are shown, for a varying number of total events. No background is assumed and all events are of signal type. For small $\ell$, the windowing function dominates and the

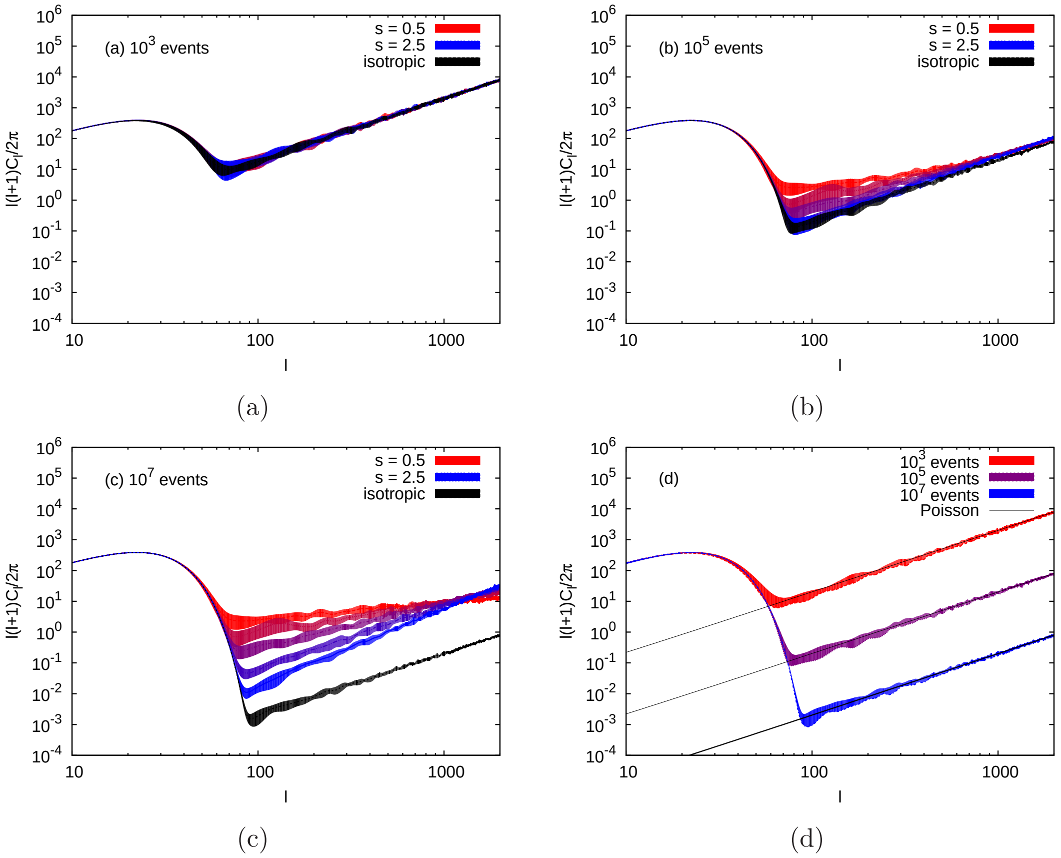

(a) (b)

(c) (d)

**Figure 1**: Angular power spectra recovered from input event maps simulated with different APS slopes $s$ from 0.5 to 2.5 in steps of $\Delta s = 0.5$ (from red to blue). In this figure, PSF effects are neglected and $\sigma_{\rm fov} = 2.5°$. No background is included in the simulations. Subfigures represent the cases of (a) $10^3$ events, (b) $10^5$ events, and (c) $10^7$ events. The effect of an increasing event number on the Poissonian noise is depicted in (d), which shows the APS of background-only simulations.

spectrum is distorted. At large $\ell$ and for a sufficiently large number of events, the signal starts to dominate, and different signal slopes can be discriminated. If the number of events is comparably small, however, the random Poissonian noise from the finite number of events will dominate the signal. The Poissonian noise is given by $C_N = 4\pi/N$ for full sky coverage (see appendix B in [9] and section IV.A in [7]), where $N = N_{\rm sig} + N_{\rm bg}$ is the total number of events. This is in good agreement with the noise estimates from the simulations of background only events (and partial sky-coverage corrected APS, see previous section), as shown in the lower right panel of Fig. 1.

The effect of the instrument's PSF on the recovered APS is illustrated in the top-left panel of Fig. 2: The PSF suppresses the signal at large $\ell$ and drives it toward the level of the Poissonian noise. The typical multipole at which the downturn happens is related

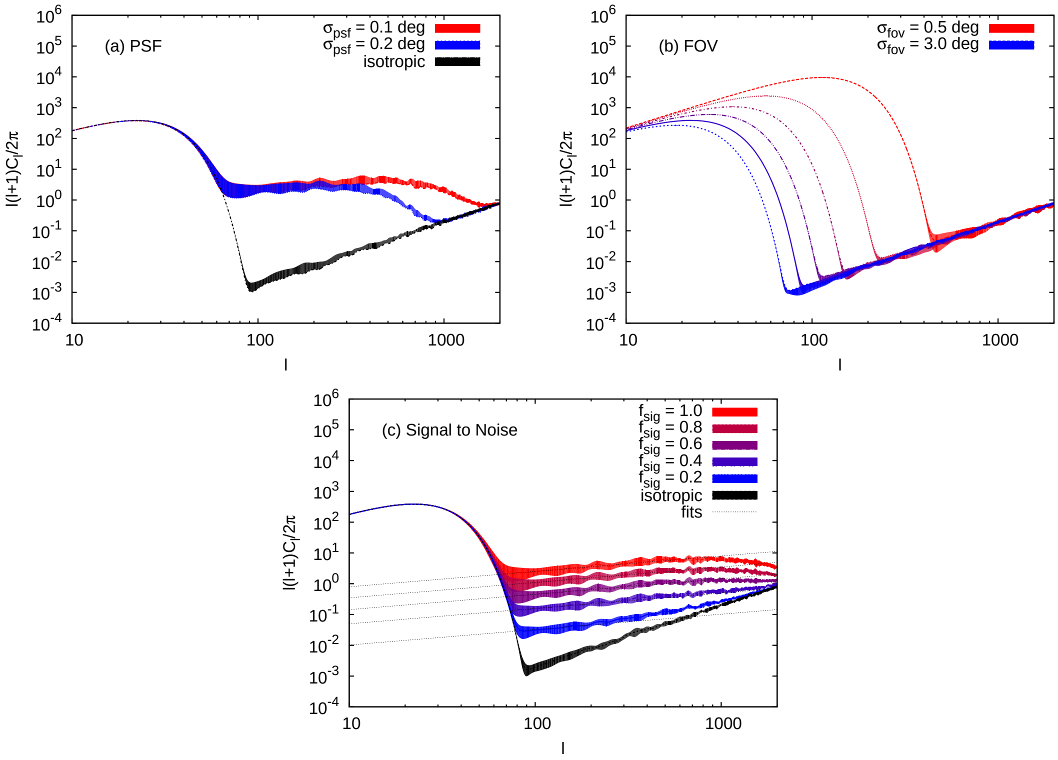

**Figure 2**: *Top left:* Effect of the PSF on the recovered APS. The slope of the input spectrum is $s = 0.5$. The PSF widths are $\sigma_{\text{psf}} = 0.1^{\circ}$ (red band) and $\sigma_{\text{psf}} = 0.2^{\circ}$ (blue band). *Top right:* Effect of the fov on the APS for a pure background (isotropic) event list, with $\sigma_{\text{psf}} = 0.05^{\circ}$. The width $\sigma_{\text{fov}}$ is increased in steps of 0.5, in the range from $\sigma_{\text{fov}} = 0.5^{\circ}$ (red) to $\sigma_{\text{fov}} = 3.0^{\circ}$ (blue). *Bottom:* Influence of the signal fraction $f_{\text{sig}}$ on the recovered APS for an input slope of $s = 0.5$; background events are distributed isotropically. Dotted lines show the APS in case of a vanishing PSF and fov distortion.

to the PSF width $\sigma_{\text{psf}}$ and given by $\ell_s \approx 180^{\circ}/\sigma_{\text{psf}}$. This effect can be corrected if $\sigma_{\text{psf}}$ (or the full PSF shape in the non-Gaussian case) is known [1], although at the expense of an increasing uncertainty of the recovered APS. In the forward-folding approach that we are using here this is, however, not necessary, since the model is directly convolved with the PSF before comparison with the (simulated) data (see Section 4).

Due to a finite fov, anisotropies at a scale larger than the fov will be suppressed. This is illustrated in the top-right panel of Fig. 2, where the APS of an isotropic (background-only) event list is shown for different fov. A larger fov allows to explore larger scales and thus lower multipoles. The minimum resolvable multipole is approximately given by $\ell_{\text{min}} \approx 180^{\circ}/\sigma_{\text{fov}}$.

The bottom panel of Fig. 2, instead, illustrates the effect of different signal-to-background fractions $f_{\text{sig}}$. The background is produced mainly by two different processes:

(i) Events caused by mostly isotropic cosmic rays (protons and electrons), which have been misclassified as photons. Anisotropies in the electron background have not been detected so far [35], while anisotropies in the hadronic background are indeed present at the level of $10^{-4}$ [36–40]. However, they extend only to a multipole of $\sim 20$ (see [36]) and are thus negligible in our analysis. For Cherenkov telescope systems the hadron background component dominates, and, therefore, a sufficiently good gamma-hadron separation is a crucial characteristic of the instrument. To reduce the residual background of cosmic-ray electrons important below a few hundred GeV, a sufficiently good gamma-electron separation would also be favorable. However, gamma-electron separation capabilities are limited, due to the similarity of electron and photon initiated showers. With current instruments a rejection of $\sim 50\%$ of the electrons seems possible [31, 32], while the expected performance of CTA on this aspect have not been studied in detail yet.

(ii) An intrinsically isotropic component of the diffuse photon background, which does not act as signal according to our definition. For instance, cosmological photons produced by truly diffuse processes may account for this background component.

Note that we do not consider the effect of the local variations of the *night-sky background* and its effect on the acceptance of the fov [33], assuming that prominent features in the fov such as bright stars can be eventually masked and excluded from the analysis. A more realistic MC simulation would be required to study the effect in detail, which is left for future work.

In the bottom panel of Fig. 2, a slope of $s = 0.5$ has been assumed for the input spectrum used to simulate the maps and event lists. Dotted lines show the recovered APS in the case of vanishing PSF effects as well as fov distortion (but with background still included). Clearly, the *background*-fraction has a large influence and considerably reduces the signal height with respect to the intrinsic Poissonian noise level, i.e. the signal-to-noise ratio. We conclude that a good *background rejection* is crucial.

Finally, we consider the effect of the observation strategy. In general, a large amount of observation time is required to detect anisotropies, and a dedicated observation could be, eventually, not feasible due to different targets competing for the limited observation time available. The use of existing observations obtained on different targets, combining them to search for anisotropies, would thus be preferable. This approach is investigated in Fig. 3. Here, $10^3$, $10^5$, and $10^7$ events are distributed within one fov and in 10 different ones. Qualitatively, when the same number of events is distributed in a single or multiple fov two effects are competing. On one hand the Poissonian noise ($=\Delta\Omega/N$ in the case of partial sky-coverage, where $\Delta\Omega$ is the covered solid angle) increases linearly with the number of fov, decreasing the sensitivity. On the other hand, with multiple fov more modes are available for the APS calculation reducing the error on the APS itself (on the sphere this effect is known as *cosmic variance*) and thus increasing the sensitivity. The overall number of events determines which error dominates (the Poissonian one or the cosmic variance ) and thus which effect is dominant.

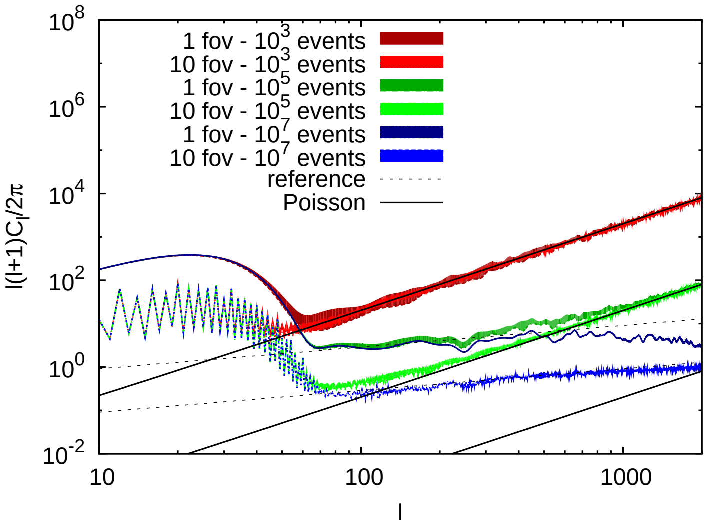

**Figure 3**: Influence of the observation strategy on the APS. Shown are the recovered APS for an input spectrum with slope $s = 0.5$ and for $10^3$ (red), $10^5$ (green), and $10^7$ (blue) events distributed in a single fov (dark colors) or 10 different fov (light colors). In all cases, the APS are normalized to the corresponding noise level, which is shown by the solid black lines. The dotted lines show the input APS for the $10^7$ events cases.

Fig. 3 illustrates that in the limit of high statistics (the $10^7$ events case), having multiple fov indeed decreases the error on the APS, indicating that the measurement is cosmic variance limited, and the sensitivity is thus improved. In the limit of low statistics ($10^3$ events), instead, the error is approximately unchanged indicating that the Poissonian noise is comparable or dominates over the cosmic variance. In this case the sensitivity is worsened or remains unchanged. Finally, the $10^5$ events case is intermediate giving a marginal improvement in sensitivity. A quantitative numerical study of this effect in a realistic scenario with background is presented in the next section. Approximate analytical formulae are given in Appendix A.

## 3 Benchmark instrumental setups and cosmic-ray backgrounds

In the following, we simulate two instrument types motivated in the first case by the characteristics of the current generation instruments such as H.E.S.S., MAGIC, and VERITAS, and in the second case by the expected properties of CTA. We also consider two threshold observation energies (100 GeV and 300 GeV) which have different signal-to-background ratios (see below and next section).

For the current generation instruments the performances below 1 TeV typically degrade rapidly in energy and we thus consider only a threshold of 300 GeV. Above 300 GeV, an effective area of $10^5\,\mathrm{m}^2$ (after selection cuts which improve the fraction of

| IACT | $E_{\rm thr} = 100\,{\rm GeV}$ | | | $E_{\rm thr} = 300\,{\rm GeV}$ | | |
|---|---|---|---|---|---|---|
| | $A_{\rm eff}$ | $\sigma_{\rm fov}$ | $\sigma_{\rm psf}$ | $A_{\rm eff}$ | $\sigma_{\rm fov}$ | $\sigma_{\rm psf}$ |
| current generation | | — | | $10^5\,{\rm m}^2$ | $1.7^\circ$ | $0.1^\circ$ |
| CTA | $10^5\,{\rm m}^2$ | $3^\circ - 5^\circ$ | $0.05^\circ$ | $3 \times 10^5\,{\rm m}^2$ | $3^\circ - 5^\circ$ | $0.05^\circ$ |

**Table 1**: Characteristics (effective area $A_{\rm eff}$, field of view $\sigma_{\rm fov}$, and PSF $\sigma_{\rm psf}$) of the instrumental setups that we use as benchmarks to perform simulations. The benchmark setups have been chosen in accordance with characteristics of the current generation of IACTs, and the planned CTA observatory. Predictions are made for two different threshold energies $E_{\rm thr}$, 100 GeV and 300 GeV.

gamma rays with respect to hadrons) is typical, together with an angular resolution of 0.1° and a fov of 1.7° (see, e.g., [23–25, 41]).

For CTA, recent Monte-Carlo studies of the expected performance [42] (see also [26, 43]) indicate an effective area of $3\times10^5\,{\rm m}^2$ above 300 GeV and $10^5\,{\rm m}^2$ above 100 GeV (see figure 15 in [42]). For both cases we assume an angular resolution of 0.05° (see figures 10 and 17 in [42]). Both effective area and angular resolution are varying functions of the energy, but to simplify the simulations we assume them to be constant. The values chosen above are the ones close to threshold energies (rather than averages in the energy range above the threshold) and thus represent a *conservative* choice, since the performances of the instrument improve with energy. Finally, for $\sigma_{\rm fov}$ we consider different choices between 3° and 5° (see table 3 in [42]). Note that the rather large fov of $\mathcal{O}(5^\circ)$ might be provided by the types C, D, and J of the suggested CTA arrays [42]. Moreover, an effectively larger fov can be achieved by a dedicated pointing pattern, adjusting the pointings of individual telescopes to correspondingly different offsets from the actual source position (see figure 3c in [26]). Table 1 summarizes the characteristics of the instruments simulated in this study. The performance of H.E.S.S.-II will be in between the two setups considered [41].

The isotropic hadronic component of the background is dependent on analysis cuts and the quality of the gamma-hadron separation. With respect to the present instruments, CTA will provide some improvement in the performance of the hadron rejection process. However, a substantial part of the background is made by cosmic-ray electrons which are more difficult to separate from gamma rays. The study in [42] provides a simulation of the total expected background from the hadronic and leptonic component, that we use to estimate the background in our setups. In particular, we refer to their Figure 16 of the integrated background rate per beam above a given energy threshold (and for the assumed effective area).

For a threshold of 100 GeV, the background-rate is in the range 0.01–0.03 Hz, which for an angular resolution of $\sim 0.1^\circ$ and a fov of 5° gives a total background rate in the range 50–150 Hz. We will thus use benchmark background rates of 10 Hz and 100 Hz, the first being slightly optimistic but still possible depending on eventual improvements of the background rejection, and the second more conservative. For a different fov the rates scale with the factor $(\sigma_{\rm fov,1}/\sigma_{\rm fov,2})^2$. For simplicity, we use 10 and 100 Hz as benchmark background rates for all the considered fov, although it should be kept in mind that for fovs of 3° and 4° the rates are over-estimated. Similarly, the background per beam for a threshold of 300 GeV is in the range $3 \times 10^{-4}$–$3 \times 10^{-3}$ Hz, and the angular resolution in the range 0.06°–0.1°, which for a fov of 5° gives background rates in the range 1.5–42 Hz. Again, we will discuss an optimistic and more conservative background-rate, i.e., 1 Hz and 10 Hz, respectively.

For the case of current IACTs (H.E.S.S., MAGIC, VERITAS), assuming the same characteristics as of CTA above 300 GeV and scaling to the smaller fov, the background rate would be reduced by a factor of 10. A further reduction in the rate is given by the smaller effective area. On the other hand, the background rejection capabilities are more limited with respect to the expectation for CTA, thus increasing the background rate. We assume the same benchmark background rates above 300 GeV as for CTA, i.e. 1 Hz and 10 Hz. These values are indeed in line with typically observed background rates.

## 4 Dark matter sensitivity

In this section, we use a more realistic setup to simulate maps with a given level of anisotropy. Here, we only consider anisotropy with a slope of $s = 2$, i.e., the same slope of the isotropic Poissonian noise. With the conventions given in section 2, $s = 2$ corresponds to an APS constant in multipole and can therefore be characterized by a single number, i.e. $C_\ell = C_P$. This kind of anisotropy spectrum, known as Poisson anisotropy, is typically expected from unresolved point sources, and is a good approximation also for most of the DM models, see [7, 8, 10–18]. The similarity to the Poissonian noise also suggests a straightforward way to simulate this kind of anisotropy. For $N$ equal sources distributed all over the sky the Poisson anisotropy of the fluctuation map will be $C_P = 4\pi/N$, and, inverting the process a map with an anisotropy equal to $C_P$ can be simulated distributing $N = 4\pi/C_P$ equal sources on the sphere. We will use this method in the following. In general, unresolved sources are not identical but have a certain flux distribution $dN/dS$. Indeed, anisotropy measurements can be used to recover the underlying $dN/dS$ [2, 5]. A simulation with a delta-like $dN/dS$ is however sufficient for the DM sensitivity study presented in the following. Once this source map is produced, we follow the algorithm described in Section 2 to produce a sequence of background or signal events. Differently from Section 2, the source maps are not rescaled, since they possess an intrinsic anisotropy normalization (the one given in input) that we want to retain.

The absolute number of background events is simply given by the integrated background rates estimated in the previous section over the observation time. For the total number of gamma rays we normalize the flux to the extrapolation above 100 GeV and 300 GeV of the spectrum of the isotropic gamma-ray background (IGRB) measured with Fermi-LAT $\phi(E) = \phi_0\,(E/100\,\mathrm{MeV})^{-2.41}$, with $\phi_0 = 1.45 \times 10^{-7}\,\mathrm{cm^{-2}\,s^{-1}\,sr^{-1}\,MeV^{-1}}$ [3], which gives the values $\phi(E > 100\,\mathrm{GeV}) \approx 6 \times 10^{-10}\,\mathrm{cm^{-2}\,s^{-1}\,sr^{-1}}$ and $\phi(E > 300\,\mathrm{GeV}) \approx 1.3 \times 10^{-10}\,\mathrm{cm^{-2}\,s^{-1}\,sr^{-1}}$. We neglect the effect of attenuation of the IGRB spectrum expected by pair production on the extragalactic background light. The expected softening in most of the attenuation models is only mild [44–50], and taking it into account would only slightly reduce the total flux above 100 GeV, while above 300 GeV the attenuation could be more pronounced. We get 10 448 and 6 659 events in total (number of events integrated over the entire field of view) for a 100 h observation with CTA, assuming a fov of 5° and a threshold of 100 GeV and 300 GeV, respectively (setups as discussed in table 1). The events are distributed between DM and astrophysical sources according to the relative contribution to the IGRB. Notice that while the number of gamma-ray events is reduced by less than a factor of 2 from a threshold of 100 GeV to 300 GeV, the number of background events is reduced by a factor of 10, due to their steeper energy spectrum and the improved background rejection at higher energies. It is thus convenient to consider a threshold of 300 GeV despite the decreasing number of events. The numbers of gamma rays and background events for all the setups are reported in table 2. The resulting signal fraction is the fraction between the signal rate and the sum of signal and background rate.

The intrinsic anisotropy of astrophysical sources is modeled in accordance to the recent measurement of anisotropy performed with Fermi-LAT in the range 1-50 GeV [1]. The fluctuation energy spectrum of the measured anisotropy is compatible with a constant value of $\sim 10^{-5}$, while the *intensity* energy spectrum of anisotropy is compatible with a power law with slope $\sim 2.4$. Combined, these results indicate that the measured anisotropy originates from unresolved blazars. This is further supported by the analysis performed in [2]. We assume that the result holds above 100 GeV and we thus use the value $C_P^A = 10^{-5}$ for the intrinsic astrophysical source anisotropies. We will however explore also other values of $C_P^A$ to assess the robustness of the results with respect to the choice of this parameter.

The theoretical predictions for the intrinsic DM anisotropy are uncertain and span over various orders of magnitude from $10^{-4}$ to $10^{-1}$. We assume a benchmark value $C_P^{DM} = 10^{-3}$ and will comment on other values. A simplified analytic calculation is reported in appendixes A, B and C, which illustrates the expected dependence of the sensitivity on the choice of $C_P^{DM}$ and $C_P^A$.

To estimate the sensitivity to the DM component, we vary the relative contribution of DM to the total IGRB flux assumed above, assigning the remaining flux to the astrophysical component. In particular, we consider five values of the DM fraction $p$, i.e., 2%, 5%, 10%, 22%, and 46%, and we interpolate the results between them. We perform 20 realizations, used to estimate the average astrophysical spectrum $C_\ell^{\rm astr}$, its error $\sigma_{C_\ell}$, and the average spectrum $C_\ell^{{\rm DM},p\%}$ composed of both the astrophysical and a fractional DM contribution of $p$. We emphasize that $C_\ell^{\rm astr} \neq 10^{-5}$ since the presence of the background alters the absolute normalization of the APS. The same consideration applies to $C_\ell^{{\rm DM},p\%} \neq 10^{-3}$.

To quantify the sensitivity to the relative DM contribution, we use a simple chi-square approach, comparing two different definitions:

$$\chi_i^2(p) = \sum_{\ell=100}^{1000} \left( \frac{C_\ell^{{\rm DM},p\%} - C_\ell^{{\rm astr},i}}{\sigma_{C_\ell}} \right)^2 , \tag{4.1}$$

$$\chi^2_j(p) = \sum_{\ell=100}^{1000} \left( \frac{C_\ell^{\mathrm{DM},p\%,j} - C_\ell^{\mathrm{astr}}}{\sigma_{C_\ell}} \right)^2 , \tag{4.2}$$

where $C_\ell^{\mathrm{DM},p\%,j}$ and $C_\ell^{\mathrm{astr},i}$ are the spectra from the single realizations as opposed to the average ones, $C_\ell^{\mathrm{DM},p\%}$ and $C_\ell^{\mathrm{astr}}$, respectively. In the estimate we use only multipoles above 100, discarding lower multipoles affected by the fov of the instrument. The chi-square $\chi^2(p)$ follows a $\chi^2$–distribution with 901 degrees of freedom, so that we can quote sensitivities at 95% confidence level (CL) for the value of $p$, for which $\chi^2(p)$ is larger than 972. However, since $\chi^2(p)$ scatters comparing different realizations, a further criterion must be specified. For example, the average value of $\chi^2_i(p)$, i.e. $\overline{\chi^2_i}(p)$, can be used. Instead, we use the more conservative requirement that at least 19 out of the 20 different $\chi^2_i(p)$ values (for a given $p$) are larger than the sensitivity threshold of 972, in order to set the value of $p$ corresponding to the 95% CL. The two different ways to define $\chi^2(p)$, see Eqs. (4.1) and (4.2), correspond to two different ways to define the sensitivity. In the first case, we assume and simulate a "true" case which has no DM contribution and we search for the minimum (at 95% CL) DM fraction required to exclude the null hypothesis. In the second case, we assume and simulate "true" cases with a DM contribution of $p$ and we search for the minimum contribution for which the null hypothesis is incompatible with the simulated data. We find the two cases to give consistent results. Let us also stress that, in both cases, our definition of sensitivity is in short a "95% CL incompatibility with the null hypothesis", which implies a comparison of two $\chi^2$-distributions. A further commonly employed definition of a sensitivity as "95% upper limit in the case of a null detection outcome of the experiment" (which requires interval estimation through a profile likelihood or test statistic procedure) can give more stringent sensitivities, but will not be used here.

Finally, we note here that the sensitivity estimation described above assumes a previous knowledge of the intrinsic astrophysical and DM anisotropies, while, in realistic cases, it would be preferable to measure these quantities from the analysis itself in order to perform a comparison with the prediction of the models. This can be done, in practice, analyzing the data in multiple bands of energies. The presence of more components at different energies and the intrinsic anisotropies of the components can then be inferred by a study of the anisotropy energy spectrum in intensity and fluctuation [13, 17]. We do not pursue such detailed analysis here, while for the sensitivity estimate to the DM contribution the above approach is sufficiently accurate.

We show the results in table 2. It is quite clear that current instruments have very limited prospects of constraining DM through anisotropies. It is worth stressing, nonetheless, that looking at anisotropies has also implications for the astrophysical sources, as we discuss in more detail below, so that this particular result should not hamper a dedicated search for anisotropies with current observatories. However, the prospects for DM searches improve for CTA, especially if the background rate can be kept reasonably under control, and sensitivities of $\sim 15\%$ and $\sim 8\%$ at 100 GeV and 300 GeV, respectively, can be achieved. Even in the most conservative case of a fov of 3°, still a sensitivity of $\sim 30\%$ above 300 GeV can be reached (not shown in the table),

**H.E.S.S./MAGIC/VERITAS $\mathbf{E_{th}}$=300 GeV $\sigma_{\mathbf{fov}} = \mathbf{1.7}^\circ$**

| Observation time [h] | Bg. rate [Hz] | Sens. | $N_{\rm sig}$ | $N_{\rm bg}$ |
|---|---|---|---|---|
| 100 | 1 | $\gtrsim$ 46% | 257 | $3.6 \times 10^5$ |
| | 10 | $\gtrsim$ 46% | | $3.6 \times 10^6$ |
| 300 | 1 | $\gtrsim$ 46% | 770 | $1.08 \times 10^6$ |
| | 10 | $\gtrsim$ 46% | | $1.08 \times 10^7$ |
| 1000 | 1 | $\gtrsim$ 46% | 2567 | $3.6 \times 10^6$ |
| | 10 | $\gtrsim$ 46% | | $3.6 \times 10^7$ |
| 10 × 100 | 1 | $\gtrsim$ 46% | 2567 | $3.6 \times 10^6$ |
| | 10 | $\gtrsim$ 46% | | $3.6 \times 10^7$ |

**CTA $\mathbf{E_{th}}$=100 GeV**

| Observation time [h] | Bg. rate [Hz] | $\sigma_{\mathbf{fov}} = \mathbf{4}^\circ$ | | $\sigma_{\mathbf{fov}} = \mathbf{5}^\circ$ | | $N_{\rm bg}$ |
|---|---|---|---|---|---|---|
| | | Sens. | $N_{\rm sig}$ | Sens. | $N_{\rm sig}$ | |
| 100 | 10 | $\gtrsim$ 46% | 6687 | $\gtrsim$ 46% | 10448 | $3.6 \times 10^6$ |
| | 100 | $\gtrsim$ 46% | | $\gtrsim$ 46% | | $3.6 \times 10^7$ |
| 300 | 10 | 30% | 20059 | 30% | 31343 | $1.08 \times 10^7$ |
| | 100 | $\gtrsim$ 46% | | $\gtrsim$ 46% | | $1.08 \times 10^8$ |
| 1000 | 10 | 30% | 66867 | 15% | 104476 | $3.6 \times 10^7$ |
| | 100 | $\gtrsim$ 46% | | $\gtrsim$ 46% | | $3.6 \times 10^8$ |
| 10 × 100 | 10 | $\gtrsim$ 46% | 66867 | 30% | 104476 | $3.6 \times 10^7$ |
| | 100 | $\gtrsim$ 46% | | $\gtrsim$ 46% | | $3.6 \times 10^8$ |

**CTA $\mathbf{E_{th}}$=300 GeV**

| Observation time [h] | Bg. rate [Hz] | $\sigma_{\mathbf{fov}} = \mathbf{4}^\circ$ | | $\sigma_{\mathbf{fov}} = \mathbf{5}^\circ$ | | $N_{\rm bg}$ |
|---|---|---|---|---|---|---|
| | | Sens. | $N_{\rm sig}$ | Sens. | $N_{\rm sig}$ | |
| 100 | 1 | 30% | 4262 | 30% | 6659 | $3.6 \times 10^5$ |
| | 10 | $\gtrsim$ 46% | | $\gtrsim$ 46% | | $3.6 \times 10^6$ |
| 300 | 1 | 30% | 12785 | 15% | 19976 | $1.08 \times 10^6$ |
| | 10 | $\gtrsim$ 46% | | $\gtrsim$ 46% | | $1.08 \times 10^7$ |
| 1000 | 1 | 15% | 42617 | 8% | 66587 | $3.6 \times 10^6$ |
| | 10 | 30% | | 30% | | $3.6 \times 10^7$ |
| 10 × 100 | 1 | 30% | 42617 | 15% | 66587 | $3.6 \times 10^6$ |
| | 10 | $\gtrsim$ 46% | | $\gtrsim$ 46% | | $3.6 \times 10^7$ |

**Table 2**: Sensitivity to detect a self-annihilating DM contribution to the IGRB, utilizing anisotropy measurements of its angular power spectrum. The sensitivity is given in terms of the minimum detectable DM gamma-ray flux, expressed in percentages of the IGRB. The three tables list the sensitivities for instrumental setups similar to current IACTs and CTA, respectively, for several observation times, background rates, fov, and observational strategies. For reference, the number of simulated signal ($N_{\rm sig}$) and background ($N_{\rm bg}$) events is listed. A value of $\gtrsim$ 46% in the table means that the sensitivity is outside our tested range.

while a fov of 4° would give a $\sim 15\%$ sensitivity.

A very interesting result is given by the sensitivity achieved with different observation strategies. As shown in table 2, the sensitivity of combining ten different

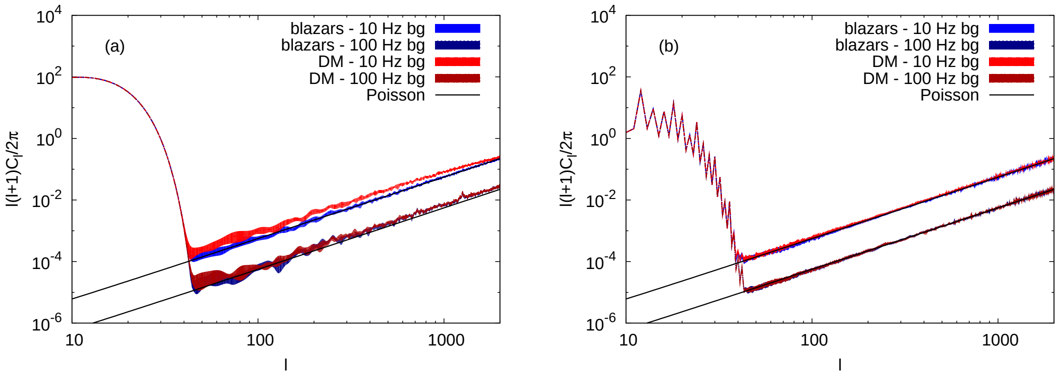

(a) Single fov, 1 000 h, $E_{\rm thr} = 100\,{\rm GeV}$ (b) Multiple fov, $10 \times 100\,{\rm h}$, $E_{\rm thr} = 100\,{\rm GeV}$

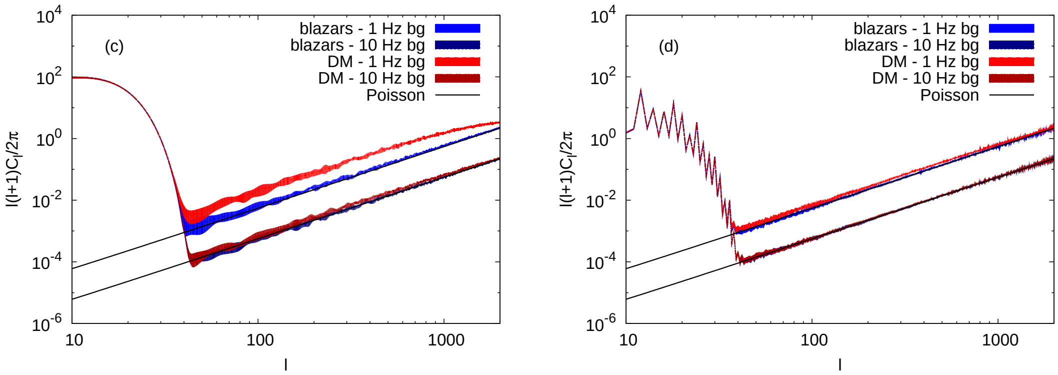

(c) Single fov, 1 000 h, $E_{\rm thr} = 300\,{\rm GeV}$ (d) Multiple fov, $10 \times 100\,{\rm h}$, $E_{\rm thr} = 300\,{\rm GeV}$

**Figure 4**: Comparison between the recovered APS for a pure astrophysical case with $C_\ell = C_P^A = 10^{-5}$ (blue bands) and a case with 46% of the total radiation originating from self-annihilating DM with $C_\ell = C_P^{DM} = 10^{-3}$ (red bands). An observation with a CTA-like telescope system of 1000 h on a single target (left column) and of 10 × 100 h splitted on 10 different targets (right column) is considered. The upper row refers to an energy threshold of 100 GeV an the lower row to 300 GeV. The two cases in each panel refer to background rates of 10 Hz and 100 Hz for 100 GeV, and 1 Hz and 10 Hz for 300 GeV. The size of the fov is $\sigma_{\rm fov} = 5°$. The lines describe the estimated noise levels.

observations of 100 h each is just a factor of 2 worse compared to a continuous 1000 h single target observation, and roughly equivalent to a full 300 h observation of a single target. Following the discussion at the end of section 2.2, this means that, even with CTA we will not be in the regime of statistics where multiple fov produce a reduction of the errors, but in the regime where the errors are comparable or slightly larger than the single fov observation. The implications of this result are, nonetheless, extremely important, since in practice the observation of a single target for 1000 h is practically not feasible (apart perhaps the Galactic Center over several years), and the observation of ten different targets for 100 h each is more likely to be realized. Most importantly, these observations do not need to be specifically targeted for anisotropy, but observations taken with different purposes can be analyzed instead. In this manner, the loss in sensitivity of a factor of $\sim 2$ would be acceptable.

The other crucial parameters determining the sensitivity are $C_P^{DM}$ and $C_P^A$. To test the dependence on these parameters, we performed a further simulation using $C_P^A = 10^{-4}$ (instead of $C_P^A = 10^{-5}$), keeping the value $C_P^{DM} = 10^{-3}$, and we found that the sensitivities decrease by a factor $\sim 3$. This seems to be in good agreement with the analytic scaling $(C_P^A/C_P^{DM})^{1/2}$ found in the appendix. Given the strong dependence on these two parameters, a firmer prediction on the sensitivity requires pinning down their uncertainties. More accurate calculations of $C_P^{DM}$ have been recently reported in [18], indicating that $C_P^{DM}$ can be as high as $10^{-1}$, dominated by the contribution of the Galactic substructures over extragalactic ones (see in particular their Fig. 7). Although such a large DM anisotropy would push the sensitivity to values better than 1%, the intrinsic emission from these very anisotropic structures is expected to be very low, as witnessed by the fact that the *intensity* anisotropies are instead dominated by the extragalactic component (see again [18]). A more accurate estimate of $C_P^A$, instead, awaits a direct measurement with Cherenkov telescopes or further work on the modeling of blazar populations at $\sim$TeV energy. In this respect, the example depicted in figure 4 shows that observation of an anisotropy $C_P^A = 10^{-5}$ is close to the sensitivity attainable with 1000 h of observation time with CTA (for the optimistic background estimate), while it would be more challenging for the splitted observation strategy. However, $C_P^A$ is not precisely known, and the possibility of a larger power such as $10^{-4}$ would obviously improve its detection capabilities, although it would imply a lower DM sensitivity. We thus propose explicit observations of these kind of anisotropies even for the current generation of instruments. Besides the possibility to constrain a DM contribution, an observation of anisotropy would provide a complementary and powerful tool to investigate astrophysical TeV sources.

Finally, we translate the sensitivity given in Table 2 as fraction of the IGRB in terms of a more common quantity, the DM self-annihilation cross section, although this introduces a further model dependence on the DM signal production model. To normalize the DM signal we use the cosmological DM model of [51] in its (optimistic) version, where DM halos have an NFW profile and the presence of DM subhalos is included (see also, e.g., [52, 53]), further boosting the annihilation signal. A less optimistic version with no substructures would give a factor of $\sim 10$ less DM annihilation flux and thus a 10 times worse sensitivity. On the other hand, using the results of [15] from the Millenium-II simulation, an order of magnitude enhancement with respect to the above "optimistic" case can be achieved with a correspondingly better sensitivity (see also [54], in particular Fig.1). The results can be seen in Fig. 5 for various annihilation channels as function of the DM particle mass $m_\chi$. The figure shows that a sensitivity to the thermal self-annihilation cross section $\langle \sigma v \rangle = 3 \times 10^{-26}\,\mathrm{cm^3 s^{-1}}$ can be reached for DM masses up to a few hundred GeV. Interestingly, even using the conservative version of the IGRB DM model above, sensitivities better than the ones achievable with dwarf spheroidal galaxies

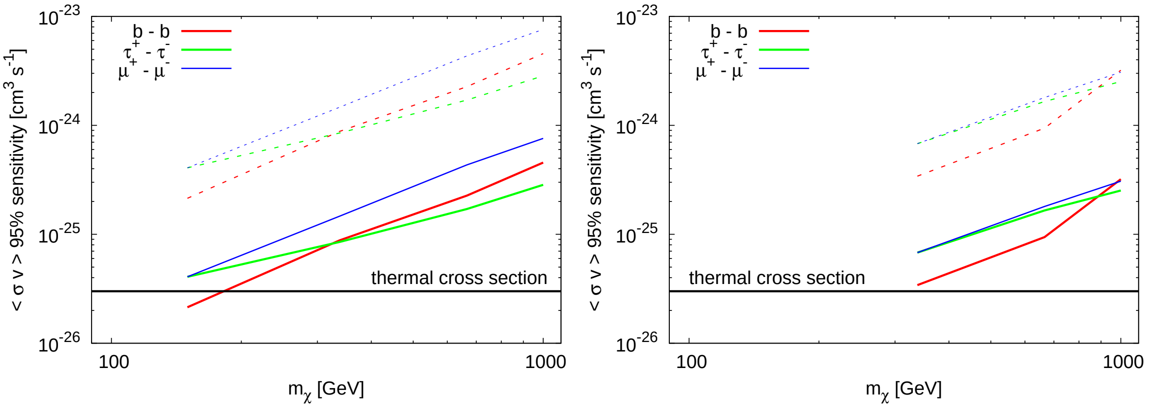

**Figure 5**: *Left:* Sensitivity of CTA on the DM self-annihilation cross section $\langle \sigma v \rangle$ as a function of the DM particle mass $m_\chi$, for an energy threshold of 100 GeV, 300 h (or 10 × 100 h) observation time, $\sigma_{\rm fov} = 5°$, and 10 Hz background rate (corresponding to $\sim 30\%$ of the IGRB in Table 2). Solid lines correspond to the model of [51] including DM annihilation in DM sub-halos, while dashed lines refer to the more conservative case of no sub-halos giving a sensitivity approximately a factor of 10 worse. We consider different annihilation channels, i.e., $b\bar{b}$ (red), $\tau^+\tau^-$ (green), and $\mu^+\mu^-$ (blue) final states. See text for more details and for the assumed instrumental characteristics. *Right:* Same as above for an energy threshold of 300 GeV, 300 h (or 10 × 100 h) observation time, and 1 Hz background rate (corresponding to $\sim 10\%$ of the IGRB in Table 2).

observed with CTA and comparable with achievable limits using clusters observations with CTA can be reached [27].

## 5 Discussion and Conclusions

With a simplified MC setup, we have investigated the key aspects of the capability of ground-based gamma-ray observatories with small fov (i.e. imaging air Cherenkov telescopes) to observe anisotropies in the diffuse gamma-ray background. In particular, we have studied the effects of the angular resolution (PSF), the field of view, and of the hadron-background rejection efficiency, which are found to be crucial characteristics for a good sensitivity to detect angular anisotropies.

Using benchmark detector configurations representing realistic setups for the present generation experiments like H.E.S.S., MAGIC, and VERITAS, and the forthcoming CTA, and using realistic expectations for the anisotropies from self-annihilating dark matter and from astrophysical sources, we have studied the sensitivity to detect a DM component through an analysis of angular anisotropies. We find that with an observation time of $\sim$1000 h and background rates of $\sim$ 10 Hz above 100 GeV and 1 Hz above 300 GeV, CTA will reach sensitivities of the order of $\sim 10\%$ to a relative contribution of DM annihilation to the total isotropic gamma-ray background. More important, we find that with a multiple field-of-view observation strategy of 1000 h splitted into ten separate targets of 100 h observations yields only a slight reduction in sensitivity ($\sim$20%, a factor of 2). This means in practice that it will be possible to obtain interesting constrains on DM without specifically dedicated deep observations, but combining instead existing observations of different primary astrophysics targets. The sensitivity achievable can be already sufficient to test the thermal annihilation cross section for DM masses $\lesssim 200$ GeV for certain models of DM annihilation in Galactic and extragalactic environments. We also find that CTA will have sufficient sensitivity to detect anisotropies from astrophysical sources with a Poisson anisotropy level of $10^{-5}$, while the sensitivity of current generation instruments is approximately one order of magnitude lower. Given the uncertainty on the exact anisotropy level expected, we nonetheless propose that available deep exposures, preferably at high galactic latitudes, should be indeed analyzed to search for anisotropies. An observation of anisotropy would provide a complementary and invaluable tool to investigate the nature of TeV sources.

## Acknowledgments

We wish to thank Mattia Fornasa and Jesus Zavala for providing suggestions on the manuscript and for useful discussions. DH acknowledges support through the collaborative research center (SFB) 676 “Particles, Strings, and the Early Universe” at the University of Hamburg.

## A Error on the Poisson Anisotropy

The error on the *fluctuation* angular power spectrum is given by

$$\delta C_\ell \equiv \sigma_\ell = (C_\ell + C_N w_\ell^2)\sqrt{\frac{2}{f_{\rm sky}(2\ell+1)}}\,, \tag{A.1}$$

where $C_N = \Omega_{\rm fov}(1/N_\gamma + N_b/N_\gamma^2)$ is the (Poisson) noise, with $N_\gamma$ the number of gamma-ray events, $N_b$ the number of background events, and $\Omega_{\rm fov}$ the total Field of View (fov) in steradians [7]; $w_\ell = \exp(\sigma_{\rm psf}^2\ \ell^2/2)$ describes the correction for a Gaussian PSF of width $\sigma_{\rm psf}$ (in radians). In the following derivation of the sensitivity, we will assume a Poisson-like spectrum, i.e. $C_\ell = C_P$. In practice, $C_P$ is estimated by calculating the weighted average of the measured angular power spectrum, so that $C_P = \sum_\ell p_\ell C_\ell$, where $p_\ell = (1/\sigma_\ell^2)/(\sum_\ell 1/\sigma_\ell^2)$ (the weight of higher multipoles is larger, owing to smaller errors, until the PSF error starts to dominate). The corresponding error on $C_P$ is the given by $(\delta C_P)^2 = \sum_\ell p_\ell^2 (\delta C_\ell)^2 = 1/(\sum_\ell 1/\sigma_\ell^2)$.

### A.1 Simple calculation

In the following, we consider both a sufficiently narrow PSF, so that the PSF correction is not crucial for the multipole range of interest, as well as the high statistics limit, so that $C_N$ is negligible with respect to $C_P$. In this limit, we have (implicitly, $\ell \gg 1$ is assumed)

$$\sigma_\ell = C_\ell \sqrt{\frac{1}{f_{\rm sky}\ \ell}}\,. \tag{A.2}$$

Evaluating the sum in $(\delta C_P)^2 = 1/(\sum_\ell 1/\sigma_\ell^2)$ (this can be done analytically or approximating the sum as an integral) yields

$$\delta C_P \approx C_P \sqrt{\frac{2}{f_{\rm sky}(\ell_{\rm max}^2 - \ell_{\rm min}^2)}} \approx \frac{C_P}{\ell_{\rm max}} \sqrt{\frac{2}{f_{\rm sky}}}\,. \tag{A.3}$$

### A.2 More accurate calculation

Assuming $\ell \gg 1$, we have

$$\sigma_\ell = (C_\ell + C_N w_\ell^2) \sqrt{\frac{1}{f_{\rm sky}\ \ell}}\,. \tag{A.4}$$

Evaluating the sum $(\delta C_P)^2 = 1/(\sum_\ell 1/\sigma_\ell^2)$ (approximating it as an integral) we find

$$\delta C_P \approx \sqrt{\frac{1}{f_{\rm sky}}} \left( -\frac{\ell_{\rm min}^2}{C_P^2} - \frac{\ln\left(C_P/C_N + w_{\ell_{\rm min}}^2\right)}{C_P^2\ \sigma_{\rm psf}^2} - \frac{1}{2\, C_P\, \sigma_{\rm psf}^2 \left(C_P + C_N w_{\ell_{\rm min}}^2\right)} \right)^{-\frac{1}{2}}. \tag{A.5}$$

With $\ell_{\rm min} \approx 100$, $\sigma_{\rm psf} = 0.05^\circ \ll 1/\ell_{\rm min} \approx 0.6^\circ$, and in the limit of high statistics ($C_P \gg C_N$), the expression can be simplified as

$$\delta C_P \approx C_P\ \sigma_{\rm psf} \sqrt{\frac{2}{f_{\rm sky}\ \ln\left(\frac{C_P}{e\, C_N}\right)}} \equiv \frac{C_P}{\ell_{\rm max}} \sqrt{\frac{2}{f_{\rm sky}}}\,, \tag{A.6}$$

which is equivalent to the previous simplified calculation with the definition $\ell_{\rm max} = \sigma_{\rm psf}^{-1} \sqrt{\ln\left(\frac{C_P}{e\, C_N}\right)}$. Note that the quantity $\ln\left(\frac{C_P}{e\, C_N}\right)$ is of order $\sim 1$ in the high statistics limit. In the case discussed in the paper, $\sigma_{\rm psf} = 0.05^\circ$ is assumed, so that the first condition is satisfied. Further, for a fov of 5° we have $\Omega_{\rm fov} \approx 10^{-2}$ sr and $f_{\rm sky} \approx 10^{-3}$. For the case of a 1000 h observation and background rate of 10 Hz above 100 GeV we have, referring to the number of events in Table 2, $C_N \approx 3 \times 10^{-5}$, while for 1 Hz above 300 GeV we have $C_N \approx 8 \times 10^{-6}$, both to be compared with $C_P = 10^{-5}$. We thus see that, even in the most optimistic cases, we are in the condition $C_P \sim C_N$. Nonetheless, for illustration purposes, in the following we will derive results in the regime $C_P \gg C_N$ to estimate the sensitivity achievable under optimal conditions.

## B Sensitivity using the intensity APS

Calculations are easier in terms of the intensity APS, since power spectra are linearly additive in case of uncorrelated summands. This is indeed the case for Poisson-like anisotropies.

The intensity APS is simply related to fluctuation APS as

$$C_P^I = I^2\, C_P, \tag{B.1}$$

where $I$ is the intensity of the component. We consider the same scenario as above, i.e., an astrophysical component with Poisson anisotropy $C_A$ and intensity $I_A$, and a DM component with anisotropy $C_{DM}$ and intensity $I_{DM}$. The corresponding intensity anisotropies are given by $C_A^I = I_A^2\, C_A$ and $C_{DM}^I = I_{DM}^2\, C_{DM}$. Assuming that the intensity anisotropy $C_P^{I,\mathrm{data}} \pm \delta C_P^{I,\mathrm{data}}$ has been measured in a given energy band, we can set a very conservative upper limit on the DM contribution as

$$C_{DM}^I \lesssim C_P^{I,\mathrm{data}}, \tag{B.2}$$

which implies

$$\frac{I_{DM}}{I} \lesssim \sqrt{\frac{C_P^{\mathrm{data}}}{C_{DM}}}. \tag{B.3}$$

If the DM component is subdominant, we have $C_P^{\mathrm{data}} \sim C_A$ and $I_{DM}/I \lesssim \sqrt{C_A/C_{DM}}$. For our benchmark case with $C_A = 10^{-5}$ and $C_{DM} = 10^{-3}$ this yields a maximum sensitivity of $I_{DM}/I \lesssim 10\%$.

A more interesting case, which more accurately approximates the case discussed with the simulations above, is when the quantity $C_P^{I,\mathrm{data}} = C_A^I$ is known within a certain error in advance, either because we have measured this quantity in a different energy band, or because it matches our theoretical expectations. In this case, a more interesting upper limit can be derived from

$$C_{DM}^I \lesssim \delta C_P^{I,\mathrm{data}}, \tag{B.4}$$

which implies

$$\frac{I_{DM}}{I} \lesssim \sqrt{\frac{C_P^{\mathrm{data}}}{C_{DM}}} \times \sqrt[4]{\frac{2}{f_{\mathrm{sky}}\ \ell_{\mathrm{max}}^2}}. \tag{B.5}$$

Again, with $C_P^{\mathrm{data}} = C_A$ and for our benchmark case $C_A = 10^{-5}$, $C_{DM} = 10^{-3}$, $\ell_{\mathrm{max}} \approx 1000$, and $f_{\mathrm{sky}} \approx 10^{-3}$, we have a maximum sensitivity of $I_{DM}/I \lesssim 2\%$. Note that the sensitivity improves with a larger fov, although only with the fourth root of it. However, the sensitivity improves faster with the angular resolution ($\ell_{\mathrm{max}}$).

We emphasize that the above results are clearly back-of-the-envelope calculations, with the purpose of estimating approximately the sensitivity and its dependence on the relevant quantities. Dealing with real data, more appropriate derivations can be conducted, for example, with a likelihood analysis.

## C Sensitivity using the fluctuation APS

In the paper, fluctuation anisotropies are used to calculate the sensitivities. In this case, the relation we are effectively imposing to derive the sensitivity is

$$C_P^{\rm data} - \delta C_P^{\rm data} \lesssim C_{\rm tot} \lesssim C_P^{\rm data} + \delta C_P^{\rm data}\,, \tag{C.1}$$

where

$$C_{\rm tot} = \frac{C_{DM} I_{DM}^2 + C_A I_A^2}{(I_{DM} + I_A)^2}\,. \tag{C.2}$$

Rewriting $C_P^{\rm data} \pm \delta C_P^{\rm data}$ as $C_P^{\rm data}\,(1 \pm \Delta)$, where $\Delta \equiv \sqrt{2/(f_{\rm sky}\ell_{\rm max}^2)}$, we find that the sensitivity is given by a second order equation, solved by

$$\frac{I_{DM}}{I_A} = \frac{C_P^{\rm data}\,(1 \pm \Delta) \pm \sqrt{C_P^{\rm data}\,(1 \pm \Delta)\,(C_A + C_{DM}) - C_A C_{DM}}}{C_P^{\rm data}\,(1 \pm \Delta) - C_{DM}}\,. \tag{C.3}$$

We can simplify the above equation in a few relevant cases. For example, if $C_{DM} \gg C_A$ (as in the benchmark case), and again assuming $C_P^{\rm data} \approx C_A$, the positive (physical) solution is

$$\frac{I_{DM}}{I} \lesssim \frac{C_P^{\rm data}}{C_{DM}} + \sqrt{\frac{C_P^{\rm data}}{C_{DM}}}\,\sqrt[4]{\frac{2}{f_{\rm sky}\ell_{\rm max}^2}}\,. \tag{C.4}$$

For the benchmark numbers we get a sensitivity of $I_{DM}/I \lesssim 3\%$, only slightly worse than in the intensity case. The sensitivity quoted in the paper for the most favorable scenario is actually 8%, therefore not very far from the analytical estimate.

Also note that for $C_A = 10^{-4}$ and $C_{DM} = 10^{-3}$ the above sensitivity degrades quite rapidly, getting worse by a factor of 10, in agreement with the simulations performed explicitly. In the intensity case, instead, the dependence is only with the square root, and the sensitivity should worsen only by a factor of $\sim$3.

Finally, unlike in the intensity case, we can get an upper limit on $I_{DM}$, even in the case $C_{DM} \ll C_A$. This case is quite unphysical, although it can be practically taken as case study for a further (non-DM) component with negligible anisotropy. This is expected, for example, from normal galaxies or truly diffuse processes like photons from UHECRs cascades on the CMB. In this case, we get

$$\frac{I_{DM}}{I} \lesssim \sqrt{\frac{2}{f_{\rm sky}\ell_{\rm max}^2}} \tag{C.5}$$

after a few simplifications, which interestingly is independent of $C_A$. The benchmark numbers for $f_{\rm sky}$ and $\ell_{\rm max}$ yield a limit of $I_{DM}/I \lesssim 5\%$.

The case $C_A \sim C_{DM}$ seems to give the worst limit. In this case, a simple formula cannot be derived and the full expression Eq. C.3 needs to be used.

## References

[1] M. Ackermann *et al.* [Fermi LAT Collaboration], Phys. Rev. D **85** (2012) 083007 [arXiv:1202.2856 [astro-ph.HE]].

[2] A. Cuoco, E. Komatsu and J. M. Siegal-Gaskins, Phys. Rev. D **86** (2012) 063004 [arXiv:1202.5309 [astro-ph.CO]].

[3] A. A. Abdo et al. [Fermi LAT Collaboration], Phys. Rev. Lett. **104** (2010) 101101.

[4] C. D. Dermer, AIP Conf. Proc. **921** (2007) 122-126 [arXiv:0704.2888 [astro-ph]].

[5] D. Malyshev and D. W. Hogg, Astrophys. J. **738** (2011) 181 [arXiv:1104.0010 [astro-ph.CO]].

[6] J. -Q. Xia, A. Cuoco, E. Branchini, M. Fornasa and M. Viel, Mon. Not. Roy. Astron. Soc. **416** (2011) 2247 [arXiv:1103.4861 [astro-ph.CO]].

[7] S. Ando and E. Komatsu, Phys. Rev. D **73** (2006) 023521;

[8] S. Ando, E. Komatsu, T. Narumoto and T. Totani, Phys. Rev. D **75** (2007) 063519;

[9] A. Cuoco, S. Hannestad, T. Haugbolle, G. Miele, P. D. Serpico and H. Tu, JCAP **0704** (2007) 013 [astro-ph/0612559].

[10] A. Cuoco, J. Brandbyge, S. Hannestad, T. Haugboelle and G. Miele, Phys. Rev. D **77** (2008) 123518;

[11] J. M. Siegal-Gaskins, JCAP **0810** (2008) 040;

[12] M. Fornasa, L. Pieri, G. Bertone, E. Branchini, Phys. Rev. **D80** (2009) 023518;

[13] J. M. Siegal-Gaskins, V. Pavlidou, Phys. Rev. Lett. **102** (2009) 241301;

[14] S. 'i. Ando, Phys. Rev. D **80** (2009) 023520 [arXiv:0903.4685 [astro-ph.CO]].

[15] J. Zavala, V. Springel, M. Boylan-Kolchin, Mon. Not. Roy. Astron. Soc. **405** (2010) 593;

[16] B. S. Hensley, J. M. Siegal-Gaskins, V. Pavlidou, Astrophys. J. **723** (2010) 277;

[17] A. Cuoco, A. Sellerholm, J. Conrad and S. Hannestad, Mon. Not. Roy. Astron. Soc. **414** (2011) 2040;

[18] M. Fornasa, J. Zavala, M. A. Sanchez-Conde, J. M. Siegal-Gaskins, T. Delahaye, F. Prada, M. Vogelsberger and F. Zandanel *et al.*, arXiv:1207.0502 [astro-ph.HE].

[19] S. Ando, E. Komatsu, T. Narumoto and T. Totani, Mon. Not. Roy. Astron. Soc. **376** (2007) 1635; F. Miniati, S. M. Koushiappas and T. Di Matteo, Astrophys. J. **667** (2007) L1

[20] J. M. Siegal-Gaskins, R. Reesman, V. Pavlidou, S. Profumo, T. P. Walker, Mon. Not. Roy. Astron. Soc. **415** (2011) 1074S.

[21] S. Ando and V. Pavlidou, Mon. Not. Roy. Astron. Soc. **400** (2009) 2122

[22] W. B. Atwood *et al.* [LAT Collaboration], Astrophys. J. **697**, 1071 (2009)

[23] F. Aharonian *et al.* [H.E.S.S. Collaboration], Astron. Astrophys. **457** (2006) 899 [astro-ph/0607333].

[24] J. Albert *et al.* [MAGIC Collaboration], Astrophys. J. **674** (2008) 1037 [arXiv:0705.3244 [astro-ph]].

[25] E. Aliu *et al.* [VERITAS Collaboration], Science **334** (2011) 69 [arXiv:1108.3797 [astro-ph.HE]].

[26] The CTA Consortium, arXiv:1008.3703 (2010).

[27] M. Doro *et al.* [CTA Collaboration], arXiv:1208.5356 [astro-ph.IM].

[28] F. A. Aharonian, A. K. Konopelko, H. J. Volk and H. Quintana, Astropart. Phys. **15** (2001) 335 [astro-ph/0006163].

[29] A. A. Abdo *et al.* [Fermi LAT Collaboration], Phys. Rev. Lett. **102** (2009) 181101 [arXiv:0905.0025 [astro-ph.HE]].

[30] M. Ackermann *et al.* [Fermi LAT Collaboration], Phys. Rev. D **82** (2010) 092004 [arXiv:1008.3999 [astro-ph.HE]].

[31] F. Aharonian *et al.* [H.E.S.S. Collaboration], Phys. Rev. Lett. **101** (2008) 261104 [arXiv:0811.3894 [astro-ph]].

[32] F. Aharonian *et al.* [H.E.S.S. Collaboration], Astron. Astrophys. **508** (2009) 561 [arXiv:0905.0105 [astro-ph.HE]].

[33] G. P. Rowell, Astron. Astrophys. **410** (2003) 389 [astro-ph/0310025].

[34] K. M. Gorski, E. Hivon, A. J. Banday, B. D. Wandelt, F. K. Hansen, M. Reinecke and M. Bartelman, Astrophys. J. **622** (2005) 759 [arXiv:astro-ph/0409513].

[35] M. Ackermann *et al.* [Fermi-LAT Collaboration], Phys. Rev. D **82** (2010) 092003 [arXiv:1008.5119 [astro-ph.HE]].

[36] R. Abbasi *et al.* [IceCube Collaboration], Astrophys. J. **740** (2011) 16 [arXiv:1105.2326 [astro-ph.HE]].

[37] R. Abbasi *et al.* [IceCube Collaboration], Astrophys. J. **746** (2012) 33 [arXiv:1109.1017 [hep-ex]].

[38] A. A. Abdo, B. Allen, T. Aune, D. Berley, E. Blaufuss, S. Casanova, C. Chen and B. L. Dingus *et al.*, Phys. Rev. Lett. **101** (2008) 221101 [arXiv:0801.3827 [astro-ph]].

[39] A. A. Abdo, B. T. Allen, T. Aune, D. Berley, S. Casanova, C. Chen, B. L. Dingus and R. W. Ellsworth *et al.*, Astrophys. J. **698** (2009) 2121 [arXiv:0806.2293 [astro-ph]].

[40] S. Vernetto *et al.* [ARGO-YBJ Collaboration], arXiv:0907.4615 [astro-ph.HE].

[41] J. Masbou, G. Lamanna and S. Rosier-Lees for the H.E.S.S. Collaboration [Proceeding of the 31 ICRC Conference, Lodz, Poland 2009], http://icrc2009.uni.lodz.pl/proc/pdf/icrc1059.pdf

[42] K. Bernlohr, A. Barnacka, Y. Becherini, O. B. Bigas, E. Carmona, P. Colin, G. Decerprit and F. Di Pierro *et al.*, arXiv:1210.3503 [astro-ph.IM].

[43] M. Martinez *et al.* [CTA Consortium Collaboration], arXiv:1111.2183 [astro-ph.IM].

[44] A. Dominguez, J. R. Primack, D. J. Rosario, F. Prada, R. C. Gilmore, S. M. Faber, D. C. Koo and R. S. Somerville *et al.*, arXiv:1007.1459 [astro-ph.CO].

[45] J. D. Finke, S. Razzaque and C. D. Dermer, Astrophys. J. **712** (2010) 238 [arXiv:0905.1115 [astro-ph.HE]].

[46] A. Franceschini, G. Rodighiero and M. Vaccari, Astron. Astrophys. **487** (2008) 837 [arXiv:0805.1841 [astro-ph]].

[47] R. C. Gilmore, R. S. Somerville, J. R. Primack and A. Dominguez, arXiv:1104.0671 [astro-ph.CO].

[48] T. M. Kneiske and H. Dole, arXiv:1001.2132 [astro-ph.CO].

[49] F. W. Stecker, M. A. Malkan and S. T. Scully, arXiv:1205.5168 [astro-ph.HE].

[50] M. Meyer, M. Raue, D. Mazin and D. Horns, Astron. Astrophys. **542** (2012) A59 [arXiv:1202.2867 [astro-ph.CO]].

[51] P. Ullio, L. Bergstrom, J. Edsjo and C. G. Lacey, Phys. Rev. D **66**, 123502 (2002) [arXiv:astro-ph/0207125].

[52] H.-S. Zechlin, M. V. Fernandes, D. Elsaesser and D. Horns, Astron. Astrophys. **538** (2012) A93 [arXiv:1111.3514 [astro-ph.HE]].

[53] H.-S. Zechlin and D. Horns, JCAP **1211** (2012) 050 [arXiv:1210.3852 [astro-ph.HE]].

[54] A. A. Abdo *et al.* [Fermi-LAT Collaboration], arXiv:1002.4415 (2010a).